Research paper

Stochastic simulation by image quilting of process-based geological models☆

Júlio Hoffimann[a,*], Céline Scheidt[a], Adrian Barfod[b], Jef Caers[c]

[a] Department of Energy Resources Engineering, Stanford University, United States
[b] Geological Survey of Denmark and Greenland, Denmark
[c] Department of Geological Sciences, Stanford University, United States

ARTICLE INFO

ABSTRACT

Process-based modeling offers a way to represent realistic geological heterogeneity in subsurface models. The main limitation lies in conditioning such models to data. Multiple-point geostatistics can use these process-based models as training images and address the data conditioning problem. In this work, we further develop image quilting as a method for 3D stochastic simulation capable of mimicking the realism of process-based geological models with minimal modeling effort (i.e. parameter tuning) and at the same time condition them to a variety of data. In particular, we develop a new probabilistic data aggregation method for image quilting that bypasses traditional ad-hoc weighting of auxiliary variables. In addition, we propose a novel criterion for template design in image quilting that generalizes the entropy plot for continuous training images. The criterion is based on the new concept of voxel reuse—a stochastic and quilting-aware function of the training image. We compare our proposed method with other established simulation methods on a set of process-based training images of varying complexity, including a real-case example of stochastic simulation of the buried-valley groundwater system in Denmark.

1. Introduction

Process-based geological models such as flume experiments (Paola et al., 2009, 2011; Straub et al., 2009; Kim et al., 2010; Tal and Paola, 2010; Paola, 2000) and advanced computer simulations of flow and sediment transport (Elias et al., 2001; Giri et al., 2008; Lesser et al., 2004) are now widely used to study the effects of geological processes in the sedimentary record. These models are known for providing more insight into physical realism compared to rule-based models (Xu, 2014; Lopez, 2003a), and are the de facto standard for addressing fundamental questions in sedimentary geology. One of the major drawbacks with the application of process-based models in practice is that they cannot be easily matched with the data acquired after deposition such as drilled wells or geophysical data. This limitation is inherent to any and all forward models, which are fully determined given well-posed boundary conditions (e.g. sea level rise, sediment supply). Furthermore, process-based geological models are complex as demonstrated by Fig. 1, demand superb modeling expertise, great amount of time (computational or laboratorial), and can be quite laborious to design (Briere et al., 2004).

In geostatistics, the process of conditioning 3D models to data has

been actively investigated (Matheron, 1963; Mariethoz and Caers, 2014). Although the research community has developed various modern algorithms in the past 15 years (Strebelle, 2002; Arpat and Caers, 2007; Zhang et al., 2006, 2015; Honarkhah and Caers, 2010; El Ouassini et al., 2008; Faucher et al., 2014; Tahmasebi et al., 2012; Mahmud et al., 2014; Yang et al., 2016; Mariethoz et al., 2010), most still have problems in handling the complexity of process-based models, suffer from low computational performance, and/or depend on non-intuitive input parameters that lack clear geological meaning. The most recent algorithms developed for geostatistical (or stochastic) simulation rely on training images from which multiple-point statistics (MPS) are reproduced (Mariethoz and Caers, 2014). Compared to alternative approaches such as object-based (Maharaja, 2008) and surface-based or event-based (Xu, 2014) simulation, training-image-based approaches have more flexible conditioning capabilities. In order to exploit process-based models as training images and condition them to data, we first need to efficiently manage their non-stationarity and arbitrary landforms.

The term non-stationarity refers to the concept that statistics vary with location and time. For example, the channel morphology in the deltaic system of Fig. 1 is a function of the distance to the delta apex. It
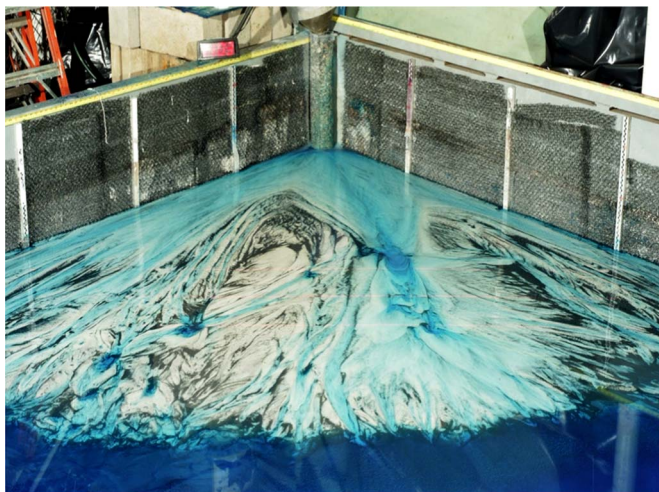
Fig. 1. Flume experiment of a delta with low Froude number performed by John Martin, Ben Sheets, Chris Paola and Michael Kelberer. Image source: https://www.esci.umn.edu/orgs/seds/Sedi_Research.htm.

is expected that channels by the sea present different characteristics compared to those evolving near the discharge point upstream in the high lands. Previous successful attempts to model non-stationarity in MPS simulation utilize auxiliary variables (Chugunova and Hu, 2008). Although effective, these attempts incorporate the variables by ad-hoc weighting; therefore, they do not scale to the complexity of 3D geological models.

Among the most used MPS simulation algorithms that model non-stationarity, we list Sequential Normal Equation Simulation (SNESIM) (Strebelle, 2002), Direct Sampling (DS) (Mariethoz et al., 2010) and Cross-correlation Simulation (CCSIM) (Tahmasebi et al., 2012). In SNESIM, probability maps that indicate the occurrence of rock facies in the subsurface are incorporated in the simulation via a probabilistic model known as the Tau model (Journel, 2002; Allard et al., 2012). Although more scientific than ad-hoc weighting, the SNESIM algorithm does not support auxiliary variables that are not probability maps. Even if adapted to handling arbitrary variables, SNESIM will still perform poorly with process-based training images because of its underlying tree structure originally developed for processing categorical values.

In DS and CCSIM, auxiliary variables are incorporated with ad-hoc weighting. As previously mentioned, this technique does not scale with complex 3D process-based models. Nevertheless, both algorithms support continuous training images and present a remarkable computational speedup compared to previous alternatives in pixel-based and patch-based stochastic simulation, respectively.

In DS, the speedup can be explained by the direct sampling of the first pattern for which the distance to the data is below a pre-specified threshold. If the threshold is large, the algorithm is fast but suboptimal. If the threshold is small, the simulation of 3D models is unfeasible. Given the resolution of process-based training images, an appropriate threshold is hardly available.

In CCSIM, the speedup can be explained by the pasting of many voxels (or pixels in 2D) at once. In this case, the choice of a threshold is less important and can be fixed to a very small value for process-based models of order $10^2 \times 10^2 \times 10^2$ voxels or larger. This quality of CCSIM is inherited from the original, seminal paper "Image Quilting for Texture Synthesis and Transfer" by Efros and Freeman (2001) who came up with the idea of quilting images in computer vision.

Efros and Freeman introduce a novel, simple, and efficient algorithm for sampling 2D images from arbitrary reference (a. k. a. training) images. In its simplest form, image quilting simulation (IQSIM) consists of 1) a raster path over which patterns (i.e. sub-images of fixed size) are pasted together with some overlap; 2) a similarity measure between patterns already pasted in the simulation

grid and patterns in the training image; and 3) a boundary cut algorithm (Boykov and Jolly, 2001; Boykov and Kolmogorov, 2001; Kwatra et al., 2003) applied in order to minimize the overlap error of the paste operation.

The Efros-Freeman algorithm addresses the texture synthesis problem. In the same paper, the authors apply image quilting for texture transfer by iterating the procedure until a mismatch with a background image is below a pre-specified threshold. The texture transfer problem is closer to the problem that is addressed in this paper, and is closer to geostatistics in general because it involves (spatial) data that needs to be honored. Their proposed iteration technique utilized by CCSIM and other variants, however; becomes computationally burdensome with 3D geological models.

Based upon the advances made by the computer vision community, Mahmud et al. (2014) extend 2D image quilting to 3D grids and attempt to incorporate hard data (or simply point data) along the raster path. The authors introduce a distance to the data and propose a weighting scheme with the distance computed in the overlap with previously pasted patterns. This scheme has two major limitations: 1) Distances must be normalized before they can be weighted and summed and 2) The weights are case-dependent and are obtained by trial and error. Although flexible, the weighting scheme proposed by Mahmud et al, and the template splitting procedure described therein, are unfeasible in real 3D applications.

In a similar attempt, Faucher et al. (2014) formulate a patch-based stochastic simulation as an unconstrained optimization where the objective function has penalty terms for hard data and local-mean histograms. In this formulation, the weights appear directly in the objective function and are chosen under a set of simplifying assumptions. Despite the very good analysis, Faucher et al assumptions may be considered too strong for arbitrary process-based training images and field data. Furthermore, there is no theoretical result that proves the existence of global weights for conditioning arbitrary random fields.

Conditioning image quilting to hard data is particularly challenging as demonstrated by all previously published attempts. The raster path is suboptimal for this task as it does not sense the data ahead in the simulation domain. In the extreme case, the data is clustered near the end of the path and is invisible to the algorithm until the very last iteration. Tahmasebi et al. (2014) alleviate the raster path issue by incorporating data ahead of the path. The proposed solution comes with an extra unknown parameter, there called the "co-template", that is not trivial to set, and yet determines the data conditioning performance. Co-templates add an unnecessary layer of complexity to grids with arbitrary landforms, and as it will be discussed in the next sections, there exists a much simpler and more effective solution.

Besides the unknown weights for combining different variables and data defined over the domain, MPS simulation algorithms usually depend on a non-trivial list of input parameters that do not convey geological nor physical understanding. In particular, the Efros-Freeman image quilting algorithm requires a window (or template) size for scanning the training image. The choice of this window can greatly affect the quality of the realizations and there is still no good criterion for its design.

In this paper, we propose a systematic probabilistic procedure for data aggregation in the original Efros-Freeman algorithm. Our proposed algorithm is faster than any other MPS simulation algorithm previously published, bypasses the ad-hoc weighting limitation, and produces visually realistic images conditioned to data. The paper is organized as follows. In Section 2, we introduce a new method for data aggregation and other minor modifications to the original Efros-Freeman algorithm to accommodate hard data (e.g. wells). In Section 3, we apply the proposed algorithm to 2D process-based and 3D process-mimicking models with real-field complexity. In Section 4, we discuss the choice of the template size in image quilting and introduce a novel criterion for template design. In Section 5, we conclude the work pointing to future research directions.
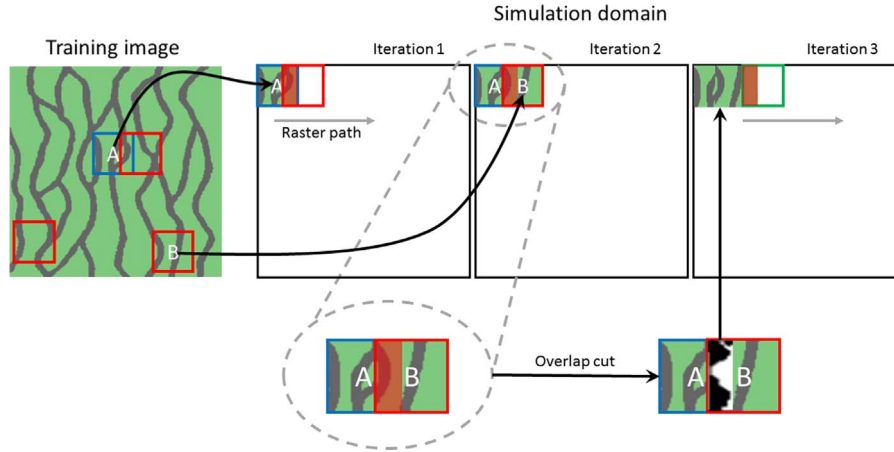
Fig. 2. Efros-Freeman algorithm. Patches are extracted from the training image and pasted in the simulation domain in raster path order. A cut is performed in the overlap with the previously pasted patch to maximize continuity. Black pixels are copied from pattern A whereas white pixels are copied from pattern B.

2. Data aggregation in image quilting

In this section, we introduce a new method for data aggregation in image quilting as an alternative to ad-hoc weighting. This method is introduced with auxiliary variables and is extended later to conditioning with hard data.

2.1. Efros-Freeman algorithm

The original Efros-Freeman image quilting for unconditional simulation is illustrated in Fig. 2. In iteration 1, a pattern "A" is randomly selected from the training image and placed in the top left corner of the simulation domain. In iteration 2, the sliding window leaves an overlap region highlighted in red. This region is compared to all regions of equal size in the training image using an Euclidean distance as measure of similarity; the next pattern "B" is drawn at random from a uniform distribution over a set of candidates colored in red (e.g. the most similar patterns). The two patterns are stitched together by means of a cut that maximizes continuity (Boykov and Jolly, 2001; Boykov and Kolmogorov, 2001; Kwatra et al., 2003). After the first row is filled, the second row is simulated similarly except that there are two overlap regions instead of one. Tile by tile the puzzle is solved. Resulting images and all the cuts performed along the path are shown in Fig. 3.

2.2. Incorporation of auxiliary variables

Consider the setup of the problem in Fig. 4 with the introduction of an auxiliary variable. A training image TI, an auxiliary variable $AUXD$ defined over the simulation domain, and a forward operator $G^*: TI \rightarrow AUXTI$ are given. The goal is to generate multiple realizations that honor the relationship established by the auxiliary variables $AUXD$ and $AUXTI$. The operator G^* approximates the mapping G used to generate the auxiliary variable $AUXD$. G may be a simple mathematical expression $G = G(i, j, k)$ in terms of the spatial indices of the grid or may consist of a series of elaborated engineering workflows that produce a property cube over the domain of interest.

Our method for data aggregation is illustrated in 2D for clarity. We start by placing a small window in the simulation domain along any overlapping path (e.g. raster path). As illustrated in Fig. 5, this placement defines a local variable $AUXD(i_t, j_t)$ for every location (i_t, j_t) in the path.

At a current location (i_t, j_t), the local variable $AUXD(i_t, j_t)$ is compared to all local variables $AUXTI(i_p, j_p)$ in the auxiliary training image. The subscript t in (i_t, j_t) refers to the few tile locations in the simulation domain whereas the subscript p in (i_p, j_p) refers to the many

pixel locations in the training image. Although there are as many variables $AUXTI(i_p, j_p)$ as there are pixels (or voxels in 3D), these local comparisons are simple Euclidean distance calculations that can be implemented very efficiently with Fast Fourier Transforms (FFTs) and Graphics Processing Units (GPUs).

Therefore, the auxiliary distances

$$D_{aux}(p) \overset{\text{def}}{=} \| AUXD(i_t, j_t) - AUXTI(i_p, j_p) \|_2^2 \tag{1}$$

are computed with a convolution pass on the auxiliary training image, similar to the procedure introduced in the original Efros-Freeman algorithm for computing overlap distances

$$D_{ov}(p) \overset{\text{def}}{=} \| Domain(i_t, j_t) - TI(i_p, j_p) \|_2^2 \tag{2}$$

at the location (i_t, j_t). While $D_{aux}(p)$ is a distance between □-shaped (i.e. rectangular-shaped) auxiliary variables, $D_{ov}(p)$ is a distance between L-shaped overlap regions.

In order to address unit and scaling issues, the distances $D_{ov}(p)$ and $D_{aux}(p)$ are converted into ranks. For a training image with N_{pat} patterns, ranks are permutations of the integers $(1, 2, ..., N_{pat})$. A permutation $(p_1, p_2, ..., p_{N_{pat}})$ is a valid rank for the distance $D(p)$ if $D(p_i) \leq D(p_j)$ for all $1 \leq i \leq j \leq N_{pat}$. Two such permutations exist, one for $D_{ov}(p)$ and another for $D_{aux}(p)$. In order to guarantee a smooth transition from the previous pattern simulated in the domain and the pattern being pasted, we introduce a tolerance for the overlap distance and use it to define an initial subset of N_{best} best candidate patterns according to the overlap information. Such tolerance is not a sensitive parameter of the algorithm and can be made arbitrarily small. In Fig. 6 we illustrate the two ranks on the training image and the reduced set of $N_{best} \ll N_{pat}$ best candidate patterns based on the overlap information.

Next, we introduce a relaxation technique whereby a subset of the N_{best} best candidate patterns is selected. This subset S contains patterns that are in agreement with both the overlap information and the auxiliary variable defined at the location (i_t, j_t). We define a chain of sets $A_1 \subseteq A_2 \subseteq \cdots \subseteq A_k$ with A_i for $i = 1, 2, ..., k$ containing the first N_i best candidate patterns according to the auxiliary variable, $N_1 \neq 0$ and $N_k = N_{pat}$. By denoting O the set of N_{best} best candidate patterns according to the overlap, the relaxation technique consists of iterating i from 1 to k until the intersection $S_i = O \cap A_i$ is non-empty. Let S be the first non-empty intersection.

The patterns in S have two ranks, one associated to $D_{ov}(p)$ and another associated to $D_{aux}(p)$. In order to draw a pattern at random we convert the ranks into probabilities with a simple linear transformation. The conditional probability of a pattern in S given its overlap rank r_{ov} is given by

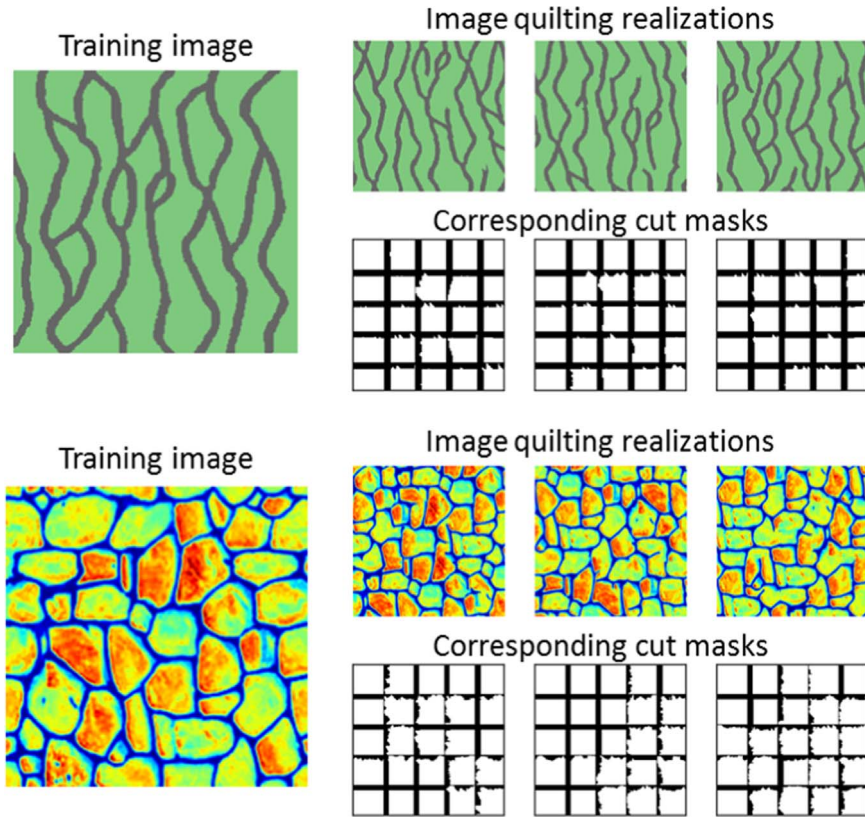$$Prob(\text{pattern}|r_{ov}) = (|S| - r_{ov} + 1)/k_{ov} \tag{3}$$

Fig. 3. Image quilting realizations of two training images and their corresponding cut masks. Texture is reproduced in both examples. Template size for binary training image is $62 \times 62 \times 1$ and template size for continuous training image is $48 \times 48 \times 1$ in the example.
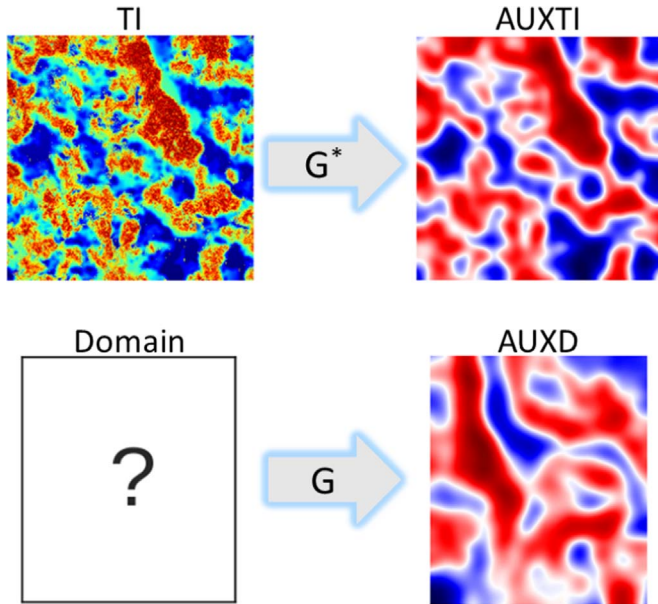

Fig. 4. Problem setup. Training image in the upper left is used to simulate the domain in the bottom left. An auxiliary variable $AUXD$ is provided over the domain as well as a proxy G^* of the forward operator G used to create $AUXD$.

Fig. 5. Proposed method (part I). Euclidean distance with "FFT trick" between current tile location (i_t, j_t) in the domain and all pixel locations (i_p, j_p) in the training image. Pattern $AUXD(i_t, j_t)$ is compared to all patterns $AUXTI(i_p, j_p)$ in a single pass.

with $|S|$ the cardinality of S and k_{ov} a normalization constant. k_{ov} is the sum of $|S| - r_{ov} + 1$ over all patterns in S. Similarly, the conditional probability of the same pattern given the auxiliary rank r_{aux} is given by

$$Prob\,(\text{pattern}|r_{aux}) = (|S| - r_{aux} + 1)/k_{aux} \qquad (4)$$

These two probabilities are combined into $Prob\,(\text{pattern}|r_{ov}, r_{aux})$ with the Tau model assuming no information redundancy (i.e. $\tau = 1$). In Fig. 7, all the patterns in S are assigned a color representing their
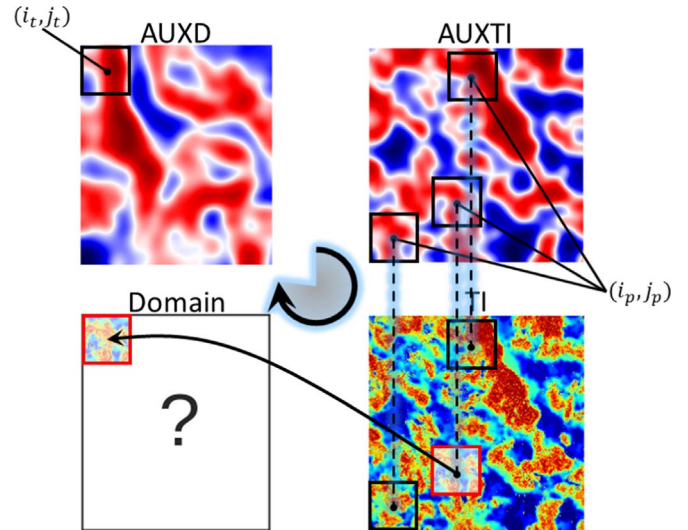
probability (e.g. $|S| = 985$). After a pattern is drawn, the entire procedure is repeated for the next location in the overlapping path.

The relaxation technique can be applied to multiple auxiliary variables. In this case, multiple chains $A_1^{(c)} \subseteq A_2^{(c)} \subseteq \cdots \subseteq A_k^{(c)}$ for $c = 1, 2, \ldots, N_c$ are run in parallel instead of one. The intersection $S_i = O \cap A_i^{(1)} \cap A_i^{(2)} \cap \cdots \cap A_i^{(N_c)}$ is guaranteed to be non-empty for some index i and the subset S is defined as before. Taking intersections of large sets is a CPU demanding operation in general, however; we exploit the fact that the maximum rank possible for a pattern is N_{pat} and implement a fast intersection algorithm for bounded sets with
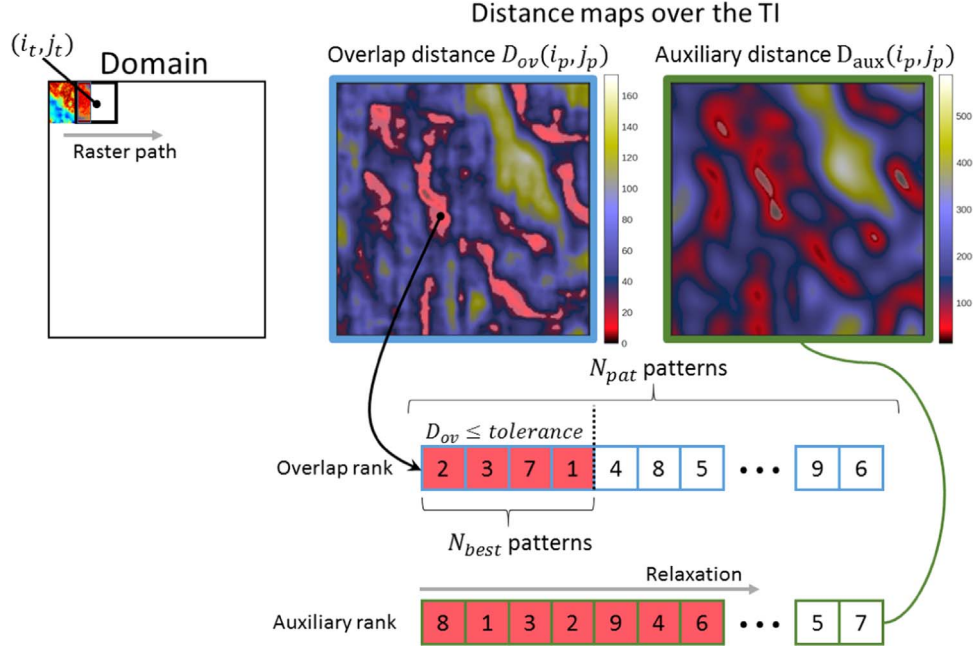
Fig. 6. Proposed method (part II). Ranking of patterns based on overlap and auxiliary distances followed by successive relaxation of auxiliary information. Given a tolerance, the best patterns are selected according to the overlap (e.g. 2, 3, 7, 1) and the set is intersected with a growing set of patterns (e.g. 8, 1, 3, …) until the intersection is non-empty.

$O(N_{pat})$ time complexity. In fact, the algorithm is a simple element-wise logical & (AND) comparison between two vectors of size N_{pat}. In Fig. 8, we compare the traditional weighting scheme with the proposed relaxation technique. Our method produces realizations that honor the auxiliary variable without the specification of weights.

2.3. Incorporation of hard data

We apply the same relaxation technique to conditioning with hard data $HD(i_t, j_t)$. Besides the distance to the overlap and to the auxiliary variables, we define a distance

$$D_{hard}(p) \overset{\text{def}}{=} \| HD(i_t, j_t) - W \odot TI(i_p, j_p) \|_2^2 \qquad (5)$$

to the point data that may exist at the current location (i_t, j_t) in the simulation domain. In Eq. (5), the matrix (or tensor in 3D) W is a mask that is only active at the pixels with datum in $HD(i_t, j_t)$, and $\odot$ is the element-wise multiplication. The ranking induced by the hard data is

combined with the other rankings through the same Tau model used for incorporating auxiliary variables.

We introduce two additional modifications to the Efros-Freeman algorithm to increase the quality of the hard data match. The first modification is the replacement of the raster path by a data-first path illustrated in Fig. 9. In this path, locations that have data are visited first and the rest of the simulation domain is filled outwards from the data using successive morphological dilations, a well known operation in image processing. We stress that this path is not related to the data-driven path described by Abdollahifard (2016), that was originally introduced by Criminisi et al. (2003).

The data-first path when applied together with the relaxation technique leads to perfect match in most data configurations. There are still two scenarios in which data is not honored: 1) the data configuration is not present in the training image and 2) the configuration is present in the training image but not in S due to conflicting ranks. We propose a simple restoration of the data (i.e. we enforce values at hard data locations) at the end of the simulation in a post-
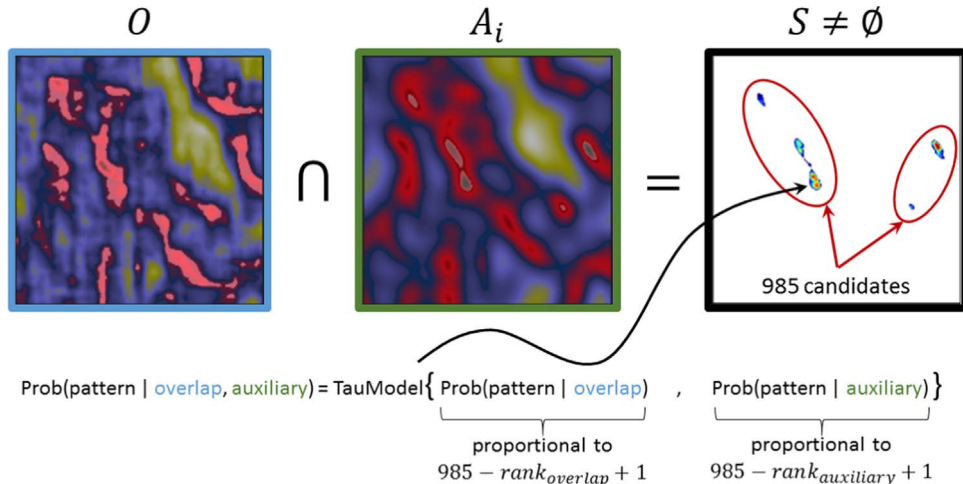

Fig. 7. Proposed method (part III). Conditional probability of pasting a pattern given both overlap and auxiliary information computed from the Tau model over all patterns in the non-empty set obtained from relaxation.
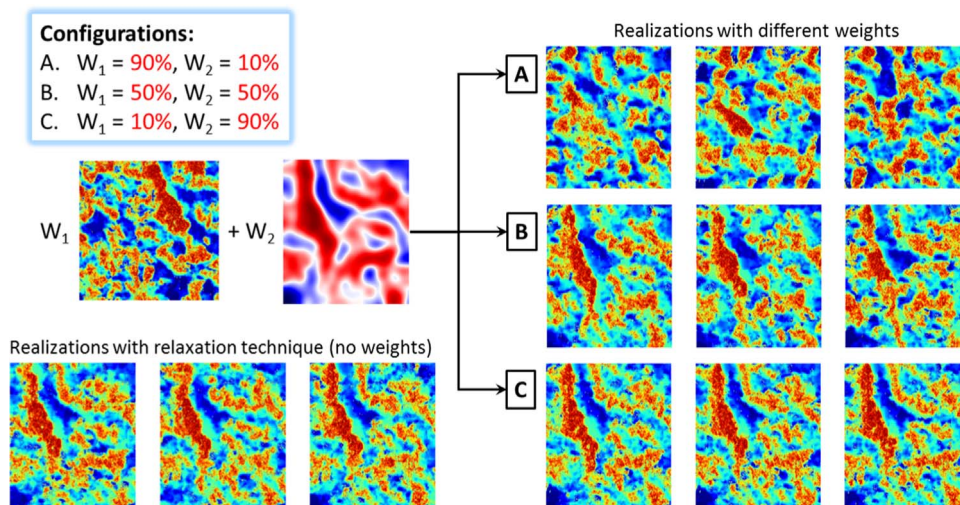
Fig. 8. Comparison of ad-hoc weighting and proposed method. Different weight configurations A, B and C leading to different conditioning results. Our method shown at the bottom left does not require specification of weights and produces the most likely outcomes given the data. Training image size: 400 × 400 × 1, Domain size: 300 × 260 × 1, Template size: 27 × 27 × 1.

processing step. Although this construction may introduce local discontinuities under very complex settings, it is effective with many realistic process-based training images.

3. Image quilting of deterministic process-based geological models

In this section, we apply the proposed method with 2D process-based and 3D process-mimicking models. Four applications of varying complexity are presented: 1) stochastic simulation of meandering rivers constrained to thickness maps, 2) spatial variability analysis with flume experiments as proposed by Scheidt et al. (2016, 2015), 3) subsurface modeling with moderately dense well configurations, and 4) completion of buried valley models with SkyTEM and partial interpretation.

Applications 1) and 2) serve to illustrate the efficiency of the relaxation technique on large 3D grids and with complex process-based training images, respectively. Application 3) highlights a known limitation of the method in the case where hard data is moderately dense. Finally, application 4) illustrates a real project in Denmark where both hard data and auxiliary variables are available.

3.1. Stochastic simulation of meandering rivers

In this application, models of a meandering river generated with the FLUMY software (Lopez et al., 2008; Lopez, 2003b) are used as training images. Our goal is to assess the performance of the relaxation technique with the Tau model on large 3D grids. We focus on a single training image with 200 × 300 × 45 cells and utilize the thickness of the basin as an auxiliary variable. This variable is introduced to minimize the appearance of channels in areas of low sediment transport.

In our method, the quality of the realizations is still a function of the template size, and because the choice of this parameter is complex, we discuss it in details in Section 4 where we propose a novel criterion for template design. By using this criterion, we select a template size of 49 × 49 × 14 and run IQSIM to obtain 50 realizations. In Fig. 10, we observe that the thickness map constrains the placement of channels to the center of the basin as intended. However, we also observe illegitimate patterns near the boundary of the realizations caused by the arbitrary landform of the model. Artifacts like these can be easily pruned with a post-processing step for a specific geometry, but the problem is still unsolved for arbitrarily shaped training images and simulation domains.

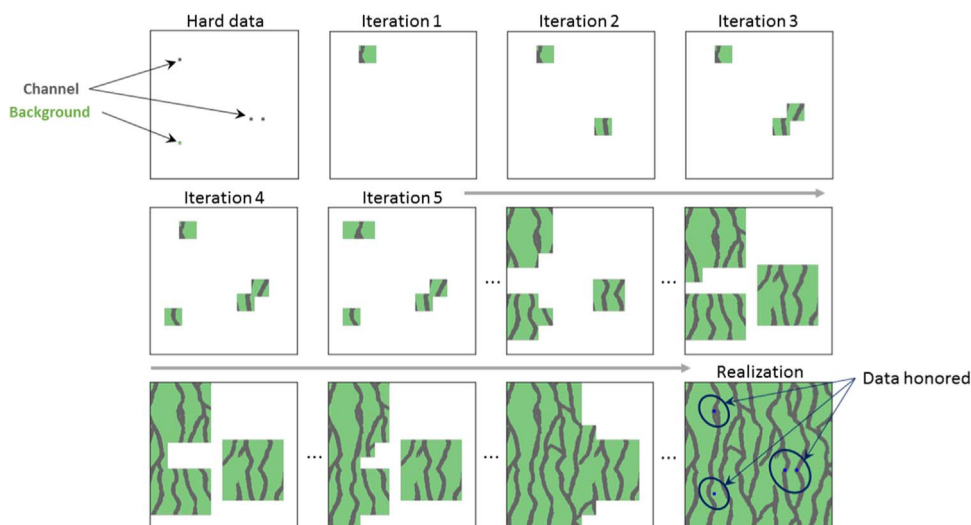A conditional simulation of the model is generated in 6 min on an

Fig. 9. Data-first path. Tiles are first pasted where hard data exists and outwards until the entire domain is filled.
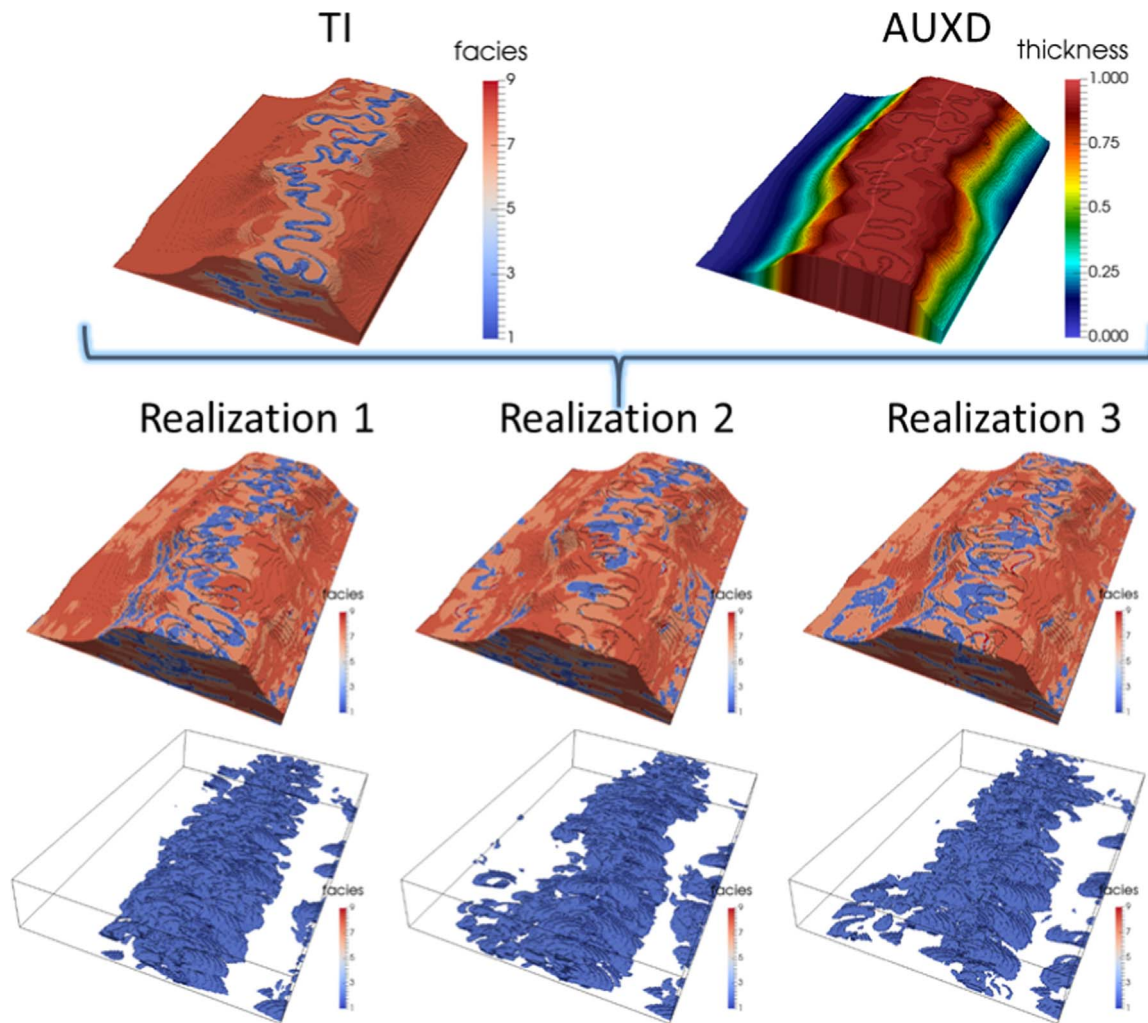
Fig. 10. Image quilting realizations of a meandering river. Realizations conditioned to thickness map have channels in the center. Artifacts observed near the boundary of the basin. Training image size: 200 × 300 × 45, Domain size: 200 × 300 × 45, Template size: 49 × 49 × 14.

integrated Intel® HD Graphics Skylake ULT GT2 GPU of a Dell XPS 13 laptop. Our algorithm and implementation are orders of magnitude faster than most (and probably all) other MPS simulation software in the literature. Besides the FFT on the GPU, we exploit the shape of the basin to save computation. For reference, alternative methods like SNESIM require many hours to handle grids of this size.

3.2. Spatial variability analysis with flume experiments

In the flume experiment provided by the St. Anthony Falls Laboratory (http://www.safl.umn.edu), we are given 136 overhead shots of a delta. Our goal is to compare the spatial variability of the given snapshots with that of image quilting realizations. We rely on the definition of a distance between these 2D models in order to quantify variability. In this work, the modified Hausdorff distance (Dubuisson, 1994; Huttenlocher et al., 1993) is investigated that only takes into account the shape of geobodies deposited in the delta.

We select a template size of 26 × 26 × 1 via the criterion discussed in Section 4 and run IQSIM with overhead shots constrained to two auxiliary variables as illustrated in Fig. 11.

The simulation is performed with 13 such snapshots (or training images) previously selected by clustering points in a multidimensional scaling projection (Scheidt et al., 2015, 2016; Borg and Groenen, 2005). For performance reasons, the modified Hausdorff distance is computed between point sets that represent the edges of the corre-

sponding geobodies as illustrated in Fig. 12. Because distances are ultimately computed between black & white images, we further run DS with the 13 intermediate binary images of the delta in order to compare the proposed algorithm with an existing software that requires fine parameter tuning.

In Fig. 13, we show the Q-Q plot between the distribution of distances originated from the experiment and the distribution of distances artificially created with geostatistics. Although the comparison of spatial variability with the modified Hausdorff distance is limited, we observe that both image quilting and direct sampling approximate the natural variability in the delta reasonably well. Outlier images exist particularly in the upper tail, and most importantly, we observe that spatial variability is usually underestimated by geostatistical simulation. This underestimation is caused by the many auxiliary variables and constraints imposed during simulation, and is depicted by the reduced interquartile range in the kernel density estimation plot in Fig. 13.

3.3. Stochastic simulation with dense well configurations

In this example, we assess the performance of the proposed method with moderately dense well configurations. The training image consists of channels generated with the Fluvsim software (Deutsch and Tran, 2002), and 9 vertical wells are placed with equal spacing in a domain of the same size as illustrated in Fig. 14.
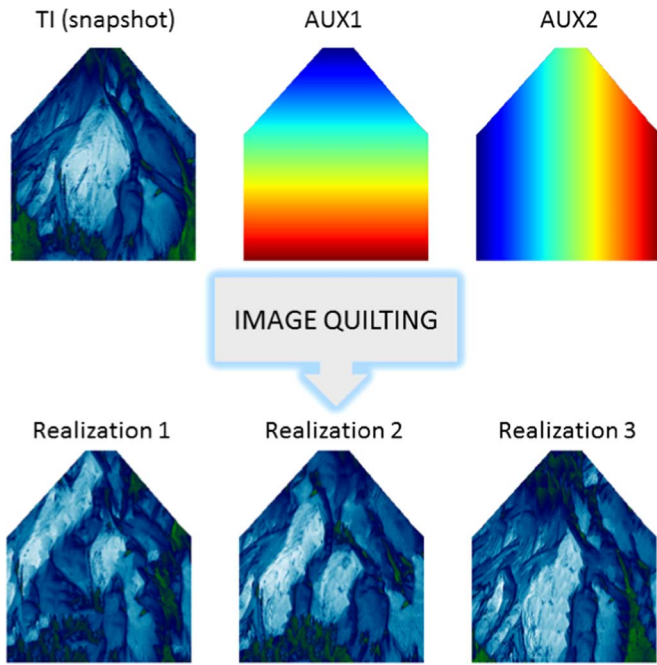
Fig. 11. Image quilting realizations of an overhead shot from the flume experiment with two auxiliary variables incorporated by proposed method. Training image size: $300 \times 260 \times 1$, Domain size: $300 \times 260 \times 1$, Template size: $26 \times 26 \times 1$.

After selecting a template size of $25 \times 25 \times 20$ via the criterion discussed in Section 4, we run image quilting and obtain 50 realizations. Three of these realizations are illustrated in Fig. 14. We observe that channels are correctly placed at the wells, but we also notice discontinuity in the generated patterns. This discontinuity is caused by the combination of the data-first path and the chosen template size, and can be quantified with various metrics as discussed in Renard and Allard (2013). We use the number and size of geobodies as metrics in Fig. 15 to illustrate the difference in connectivity between the training image and the IQSIM realizations for this well configuration.

Reducing the template size to accommodate the wells is a valid strategy, but it increases the computational time and can diminish the performance of the simulation to that of alternative methods.

In Fig. 16, we illustrate the ensemble average and variance of the 50 realizations. High average and low variance at the well locations are guaranteed by design.
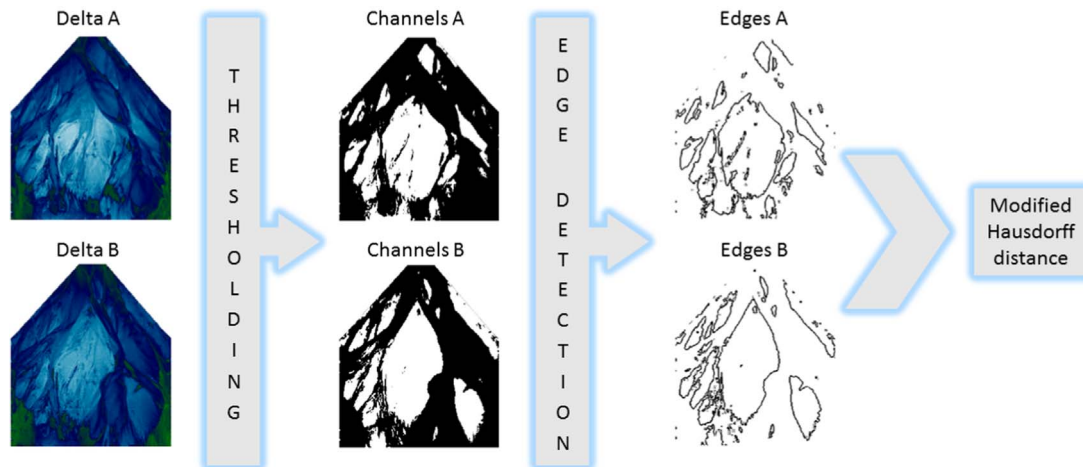
3.4. Completion of buried valleys with SkyTEM and partial interpretation

A collection of buried valleys interpreted from SkyTEM measurements (Sørense and Auken, 2004) in Denmark is used to illustrate the application of our method in a case with real field complexity. In Fig. 17, we show a single 3D model with $229 \times 133 \times 39$ voxels interpreted by hydrologists that are working on mapping groundwater in the country (Thomsen et al., 2004; Høyer et al., 2015).

To test our method in this real field case, we propose an experiment in which we assume that half of the interpretation is unavailable. In the first case, we use the patterns in the left half of the model to simulate the right half "$L \rightarrow R$". In the second case, we revert the setup "$R \rightarrow L$" as illustrated in Fig. 18.

In this experiment, we have hard data conditioning—the known half of the interpretation—and the SkyTEM measurements as an auxiliary variable. For each case, we generate 50 realizations with a template size of $49 \times 49 \times 18$. Realizations of the valleys are shown in Fig. 19 for the setup "$L \rightarrow R$".

In Fig. 20, we show the average of indicator variables (a probability) defined for the first two categories of the training image—sand & gravel and coarse clay. The third category corresponding to the background red color—hemipelagic clay—is omitted. We observe that many geobodies are correctly recovered from the SkyTEM data, but that a limited number of patterns in the training image can only approximate the other half of the most likely interpretation.

For the case "$L \rightarrow R$", we run SNESIM with a set of tuned parameters. Similar to the comparison of IQSIM and DS in the 2D flume experiment, we want to emphasize that our method does not require fine parameter tuning for producing decent results. In Fig. 21, we illustrate the distribution of modified Hausdorff distances per category computed between each of the 50 realizations and the most likely interpretation from SkyTEM. The distribution obtained with the two methods is compared on a per-category basis.

Image quilting realizations present lower distances in distribution and better reproduce the texture of the training image. For this specific setup, a single realization is generated in 3 min with IQSIM on an Intel® HD Graphics Skylake ULT GT2 GPU versus 30 min with SNESIM on an Intel® Core™ i7-6500U CPU. For completeness, another realization is generated in 5 min with IQSIM on the same CPU.

4. Criterion for template design

In this section, we introduce a novel criterion for choosing template configurations in image quilting. We start by motivating the criterion
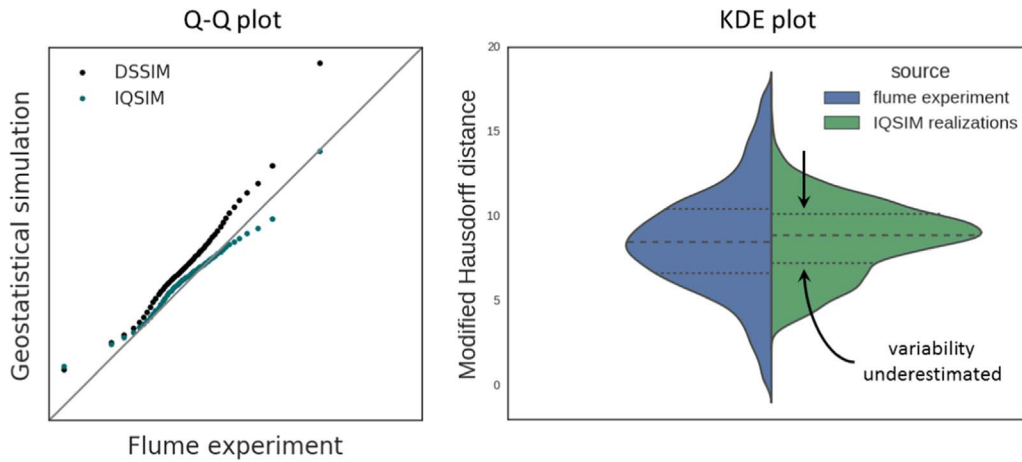

Fig. 12. Distance calculation between images. First, images are threshold to wet/dry binary images. Second, an edge filter is applied to produce a reduced set of points. Finally, the Modified Hausdorff distance is computed between the resulting point clouds.

Fig. 13. Comparison of natural variability present in the flume experiment with variability created by means of geostatistical simulation. Presence of outliers in the upper tail of the distribution. Underestimation of spatial variability depicted by reduced interquartile range.

with a simple example in 2D where we compare image quilting realizations of two different training images. Next, we state the proposed criterion as an optimization problem and derive an efficient approximation that is solved in low CPU time. Finally, we compare the criterion with the traditional entropy plot and assess its robustness with basic checks and well-known training images.

In Figs. 22 and 23, we illustrate a few image quilting realizations of 2D training images with different template configurations. In this example, template configurations are squares of the form $(T, T, 1)$ with T the template size in pixels. We observe that different template sizes lead to different texture in the realizations. For the channelized training image, increasing the template size from $T = 12$ to $T = 63$ improves the results, whereas for the Gaussian training image, the improvement is obtained by decreasing from $T = 82$ to $T = 32$.

The interesting observation is that a measure for template selection based on a monotonically increasing measure (e.g. entropy (Tahmasebi and Sahimi, 2012; Journel and Deutsch, 1993; Honarkhah and Caers, 2010)) is suboptimal. We propose a function inspired by the principle of minimum energy from thermodynamics. This principle can be rephrased in the context of image quilting as follows:

A good image quilting simulation pastes patterns sequentially

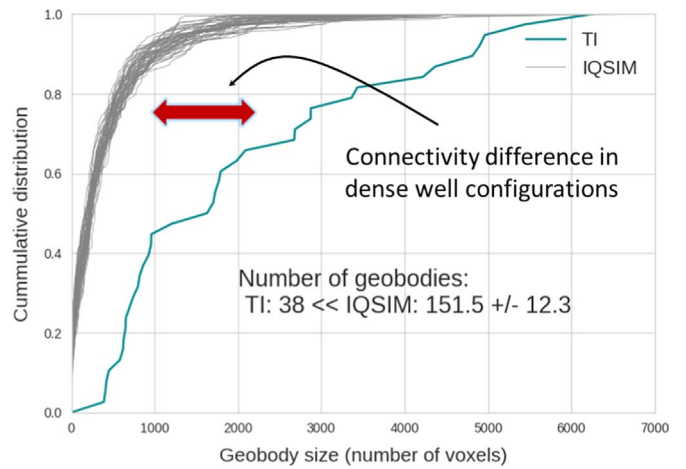without overwriting what was already pasted in previous iterations.

Fig. 15. Cumulative distribution of geobody size for a moderately dense well configuration. Positive skewed distributions for image quilting realizations indicate pattern discontinuity compared to the training image.
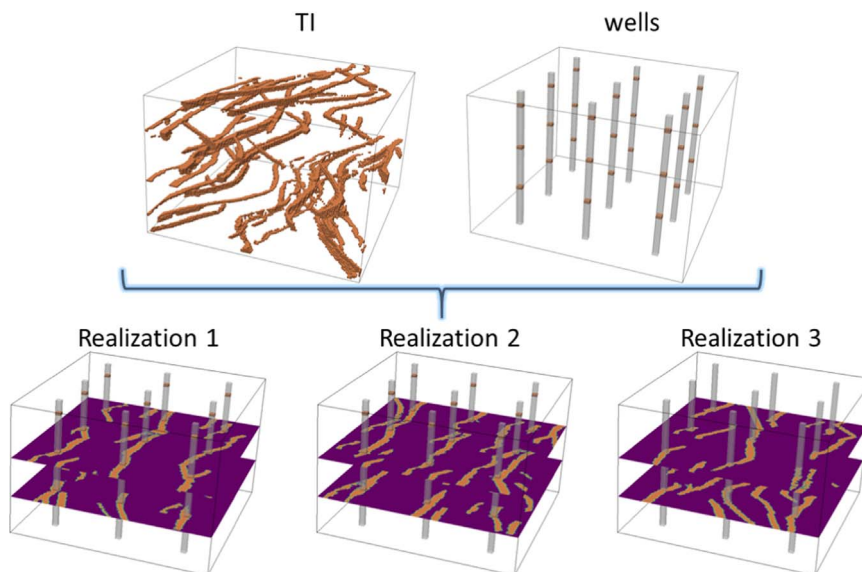

Fig. 14. Image quilting realizations of fluvial river channels conditioned to 9 vertical wells. Placement of channels illustrated on horizontal slices. Training image size: $250 \times 250 \times 100$, Domain size: $250 \times 250 \times 100$, Template size: $25 \times 25 \times 20$.
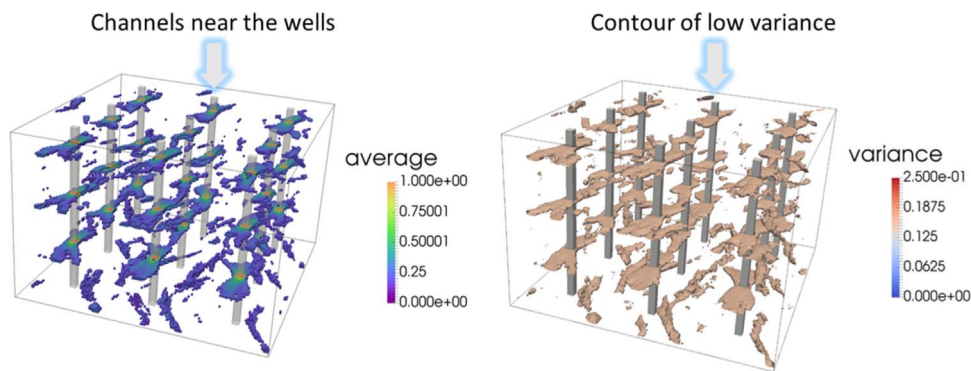
Fig. 16. Ensemble average and variance over 50 realizations. Channels placed where indicated in the wells and corresponding low variance.
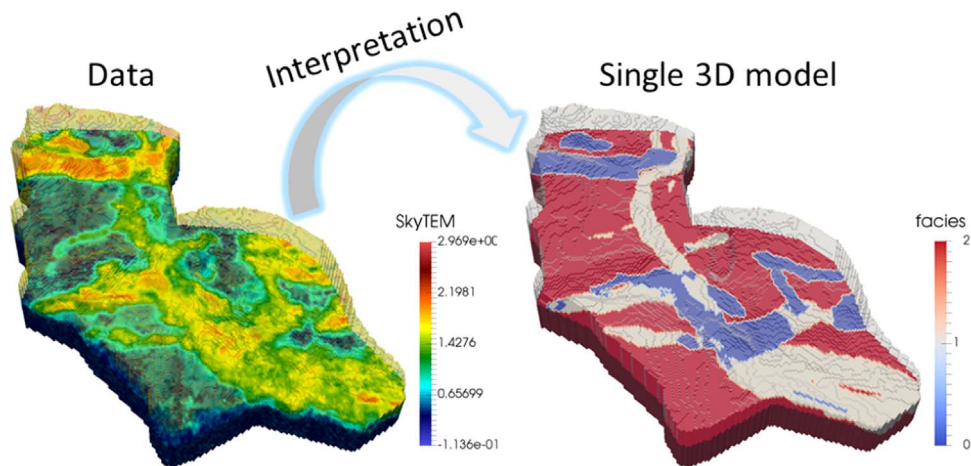

Fig. 17. Single interpretation of buried valleys from SkyTEM measurements. Resulting model has three categories: 0) sand & gravel—quaternary meltwater sand and sand till, Miocene sand, and quaternary buried valleys infilled with sand, 1) coarse clay—quaternary clay till, meltwater clay and buried valleys infilled with clay and clay till, and 2) hemipelagic clay—hemipelagic, fine grained Paleogene and Oligocene clays.
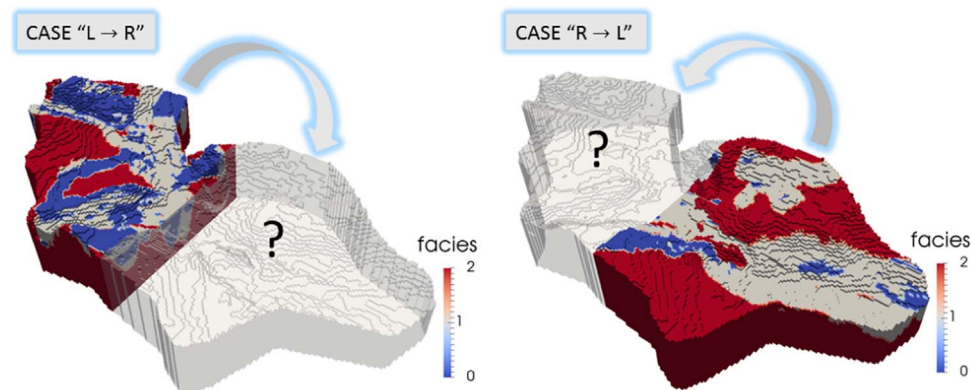

Fig. 18. Experiment setup. Half of the interpretation is discarded and then simulated with image quilting. The known half is used as hard data and the SkyTEM measurements are incorporated as an auxiliary variable.

The motivation for this principle is better understood by considering the boundary cuts in Fig. 24. According to the principle of minimum energy (or overwrite), the quilting algorithm should be designed to maximize the number of black pixels in the overlap region, which is only invaded by white pixels when there is misalignment of the pattern coming from the training image and the patterns already pasted along the overlapping path.

Definition (*voxel reuse***).** The voxel (or pixel in 2D) reuse $\mathcal{V}_{\circlearrowleft} \in [0, 1]$ of an image quilting realization is the number of black voxels in the boundary cut divided by the total number of voxels in the overlap region.

For a fixed template size to overlap ratio (e.g. 6 ÷ 1), the voxel reuse

is a function of the template size $\mathcal{V}_{\circlearrowleft}(T)$. We seek its maximum, or alternatively, the minimum overwrite defined as the complement $1 - \mathcal{V}_{\circlearrowleft}(T)$. Because the function is stochastic we formally state the optimization in terms of mean voxel reuse:

$$T^* = \underset{T}{\mathrm{argmax}}\ \mathbb{E}[\mathcal{V}_{\circlearrowleft}(T)] \tag{6}$$

We argue that, given a set of image quilting realizations generated with template size T and their corresponding boundary cuts, the number $\mathbb{E}[\mathcal{V}_{\circlearrowleft}(T)] \in [0, 1]$ is a measure of texture reproduction. Consequently, the multiple optima T^* are also the solution to the template design problem. In Fig. 25, we illustrate the mean voxel reuse as a function of the template size for a few training images in our
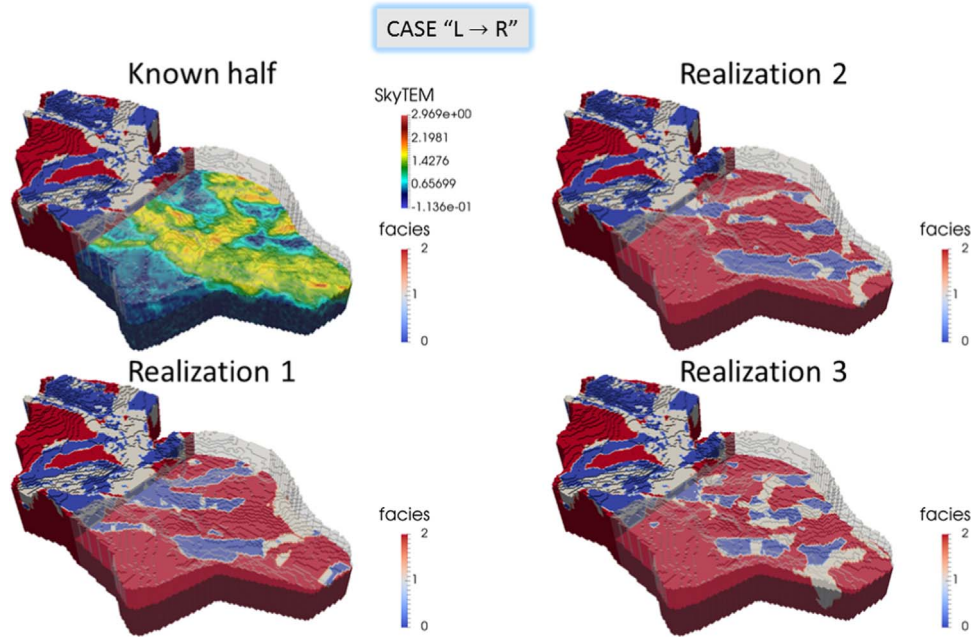
Fig. 19. Image quilting realizations of buried valleys conditioned to SkyTEM measurements and known half of the basin. Training image size: $229 \times 133 \times 39$, domain size: $229 \times 133 \times 39$, Template size: $49 \times 49 \times 18$.
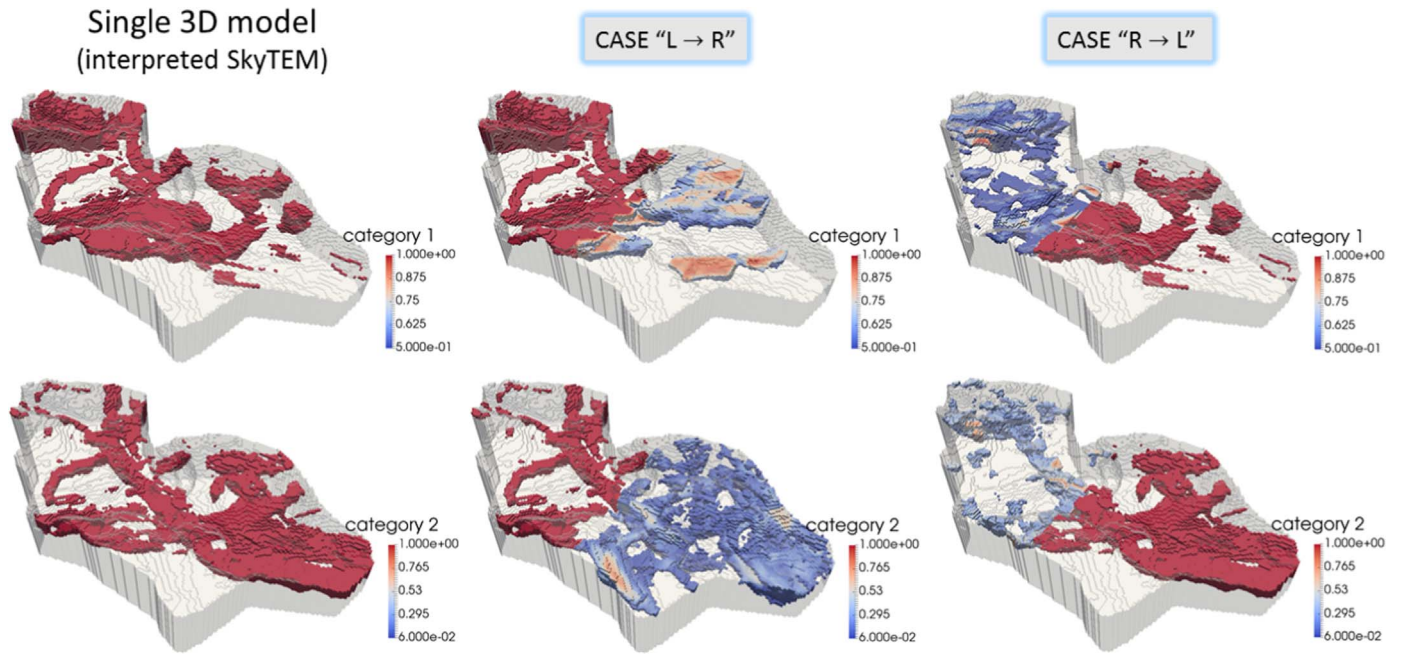

Fig. 20. Ensemble average of indicator variables for categories 1 and 2. Single 3D model interpreted from SkyTEM illustrated in the first column for reference.

library. We observe that the mean voxel reuse generalizes the Shannon entropy to continuous training images.

The plots in Fig. 25 were generated by brute force: for each template size T we generated 10 unconditional image quilting realizations with the same size of the training image and averaged the voxel reuse. However, an estimate of mean voxel reuse does not require full simulation, only a few boundary cuts performed with the training image. We derive a fast approximation with the notion of *elementary overlapping paths* as follows.

Given any 3D template configuration (T_x, T_y, T_z), the most simple path that exhibits all overlap combinations has $2 \times 2 \times 2$ tiles (or blocks), it is shown in Fig. 26. For the vast majority of the lookups in the training image that consider the overlaps x, y and z separately, there exists a perfect pattern match. We can assume no overwrite

$\mathbb{E}[\mathcal{V}_\circ^x] = \mathbb{E}[\mathcal{V}_\circ^y] = \mathbb{E}[\mathcal{V}_\circ^z] = 1$ and conclude that these boundary cuts are irrelevant to the estimate of the mean voxel reuse. On the other hand, the combinations xy, xz, yz and xyz, at which misalignment is likely to happen, contain valuable information (e.g. $\mathbb{E}[\mathcal{V}_\circ^{xy}]$ is a function of the texture).

We consider the average over a few N elementary overlapping paths (i.e. $2 \times 2 \times 2$ tiles) in Eq. (7) and discuss the implications of using this average instead of averaging full image quilting realizations.

$$\mathbb{E}[\mathcal{V}_\circ] \approx \frac{1}{N} \sum_{k=1}^{N} \mathcal{V}_{\circ,k} \tag{7}$$

The voxel reuse of an elementary overlapping path can be decomposed into its different overlap combinations:
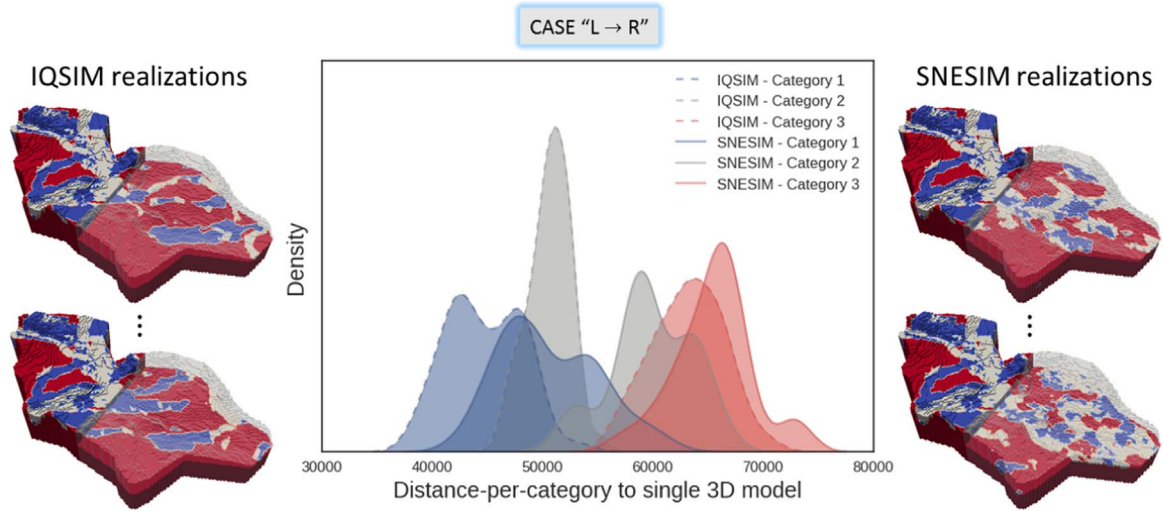
Fig. 21. Distance-per-category between geostatistical realizations and single 3D model interpreted from SkyTEM. Image quilting (IQSIM) presents lower distances in distribution than single normal equation simulation (SNESIM).
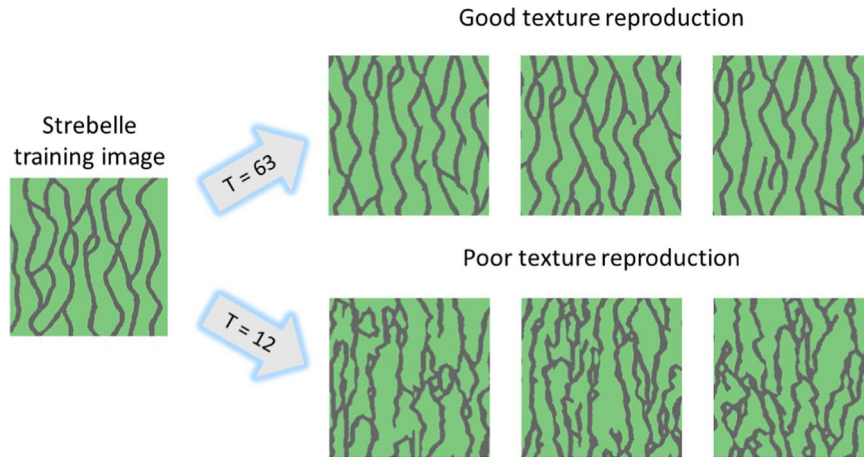

Fig. 22. Image quilting realizations of Strebelle training image. Texture reproduction improves by **increasing** template size.
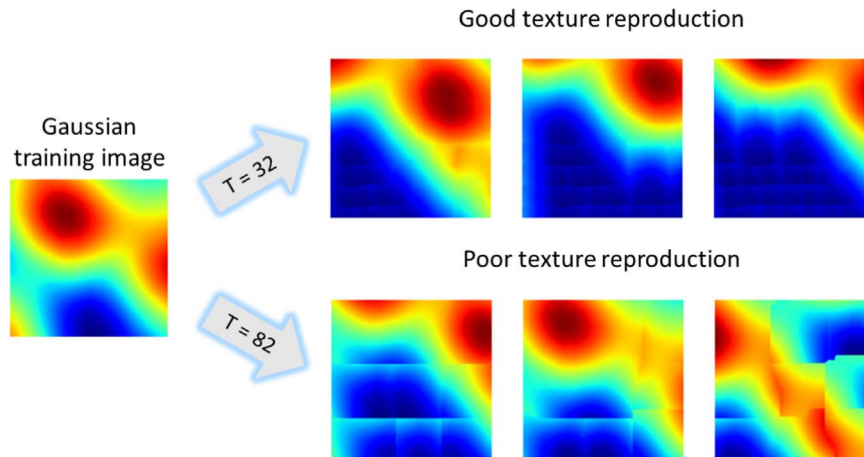

Fig. 23. Image quilting realizations of Gaussian training image. Texture reproduction improves by **decreasing** template size.

$$\mathcal{V}_{\circlearrowleft} = f_x \mathcal{V}_{\circlearrowleft}^x + f_y \mathcal{V}_{\circlearrowleft}^y + f_z \mathcal{V}_{\circlearrowleft}^z + f_{xy} \mathcal{V}_{\circlearrowleft}^{xy} + \cdots + f_{xyz} \mathcal{V}_{\circlearrowleft}^{xyz} \tag{8}$$

where f_c is the fraction of the overlap volume associated to the combination $c \in C = \{x, y, z, xy, xz, yz, xyz\}$. Denote (T_x, T_y, T_z) the template size and (o_x, o_y, o_z) the overlap. There are $(2T_x - o_x) \times (2T_y - o_y) \times (2T_z - o_z)$ voxels in the path or $n_x \times n_y \times n_z$ for short. We can write fractions of the overlap volume V_{ov} in terms of

these geometrical parameters, for example:

$$f_x = \frac{V_x}{V_{ov}} = \frac{o_x T_y T_z}{n_x n_y n_z - (n_x - o_x)(n_y - o_y)(n_z - o_z)} \tag{9}$$

Thus, the terms in the expansion $\mathcal{V}_{\circlearrowleft} = \sum_{c \in C} f_c \mathcal{V}_{\circlearrowleft}^c$ introduced in Eq. (8) are a product of geometric factors f_c times texture terms $\mathcal{V}_{\circlearrowleft}^c$. The mean voxel reuse is given by:
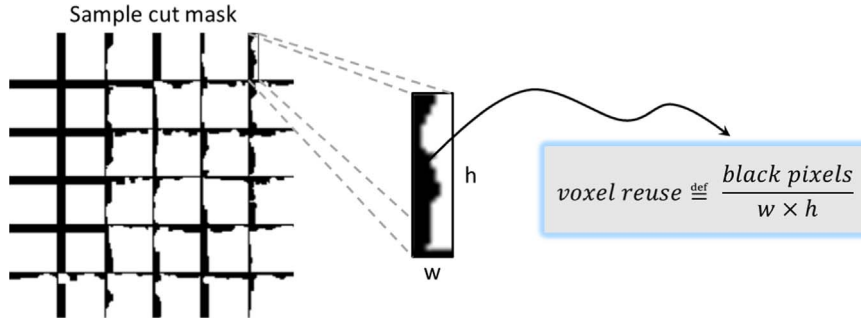
Fig. 24. Zoom in 2D boundary cut mask. Voxel reuse defined as the number of black pixels divided by overlap area.
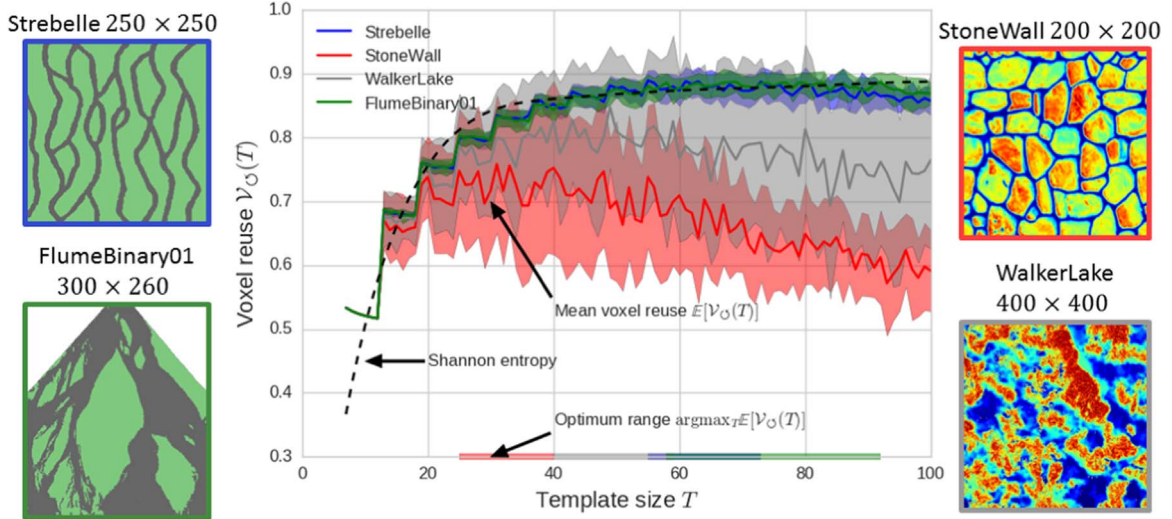

Fig. 25. Mean voxel reuse (solid line) and standard deviation (colored area) for a few training images in our library. Generalization of Shannon entropy (dashed line) to continuous training images. (For interpretation of the references to color in this figure legend, the reader is referred to the web version of this article.)
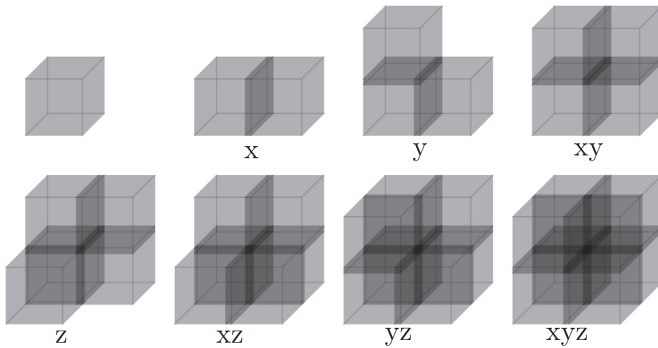

Fig. 26. Elementary overlapping path. $2 \times 2 \times 2$ tiles stitched together.

$$\mathbb{E}[\mathcal{V}_{\circlearrowleft}] = \sum_{c \in C} f_c \mathbb{E}[\mathcal{V}_{\circlearrowleft}^c]$$

$$= f_x + f_y + f_z + \sum_{c \in \{xy,xz,yz,xyz\}} f_c \mathbb{E}[\mathcal{V}_{\circlearrowleft}^c] \qquad (10)$$

We first consider the 2D case where we have $\mathbb{E}[\mathcal{V}_{\circlearrowleft}] = f_x + f_y + f_{xy}\mathbb{E}[\mathcal{V}_{\circlearrowleft}^{xy}]$. If instead of 2×2 tiles we had $m_x \times m_y$ tiles in the path, the derived expression would be

$$\mathbb{E}[\mathcal{V}_{\circlearrowleft}] = (m_x - 1)f_x + (m_y - 1)f_y + f_{xy} \sum_{i=1}^{(m_x-1)(m_y-1)} \mathbb{E}[\mathcal{V}_{\circlearrowleft}^{xy,i}] \qquad (11)$$

with the variable i looping over all tiles for which both cuts in x and y are performed. Eq. (11) can be further simplified to

$$\mathbb{E}[\mathcal{V}_{\circlearrowleft}] = (m_x - 1)f_x + (m_y - 1)f_y + (m_x - 1)(m_y - 1)f_{xy}\mathbb{E}[\mathcal{V}_{\circlearrowleft}^{xy}] \qquad (12)$$
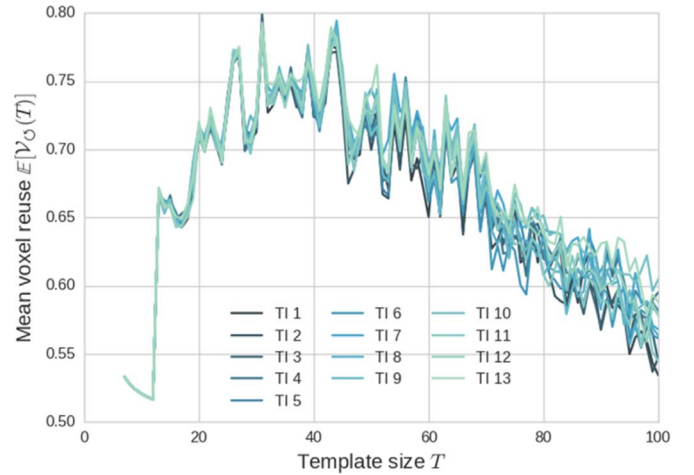

Fig. 27. Mean voxel reuse for different overhead shots of the flume experiment. All curves match except for small fluctuations.

if we assume that the texture is the same everywhere in the training image (i.e. 1st-order stationary random process assumption). Notice that the fractions f_c are a function of the number of tiles $m_x \times m_y$ in the realization, but are *not* a function of the template size (T_x, T_y). Eq. (12) can be rewritten in a simpler form $\mathbb{E}[\mathcal{V}_{\circlearrowleft}] = a_0 + a_1 \mathbb{E}[\mathcal{V}_{\circlearrowleft}^{xy}]$ with a_0 and a_1 functions of the overlapping path size.

The effects of a_0 and a_1 in the mean voxel reuse plot are vertical shift and scaling, respectively. These operations do not affect the locations of the maxima $T^* = \text{argmax}_T \mathbb{E}[\mathcal{V}_{\circlearrowleft}(T)]$ and this proves that the use of elementary overlapping paths for template design of 2D
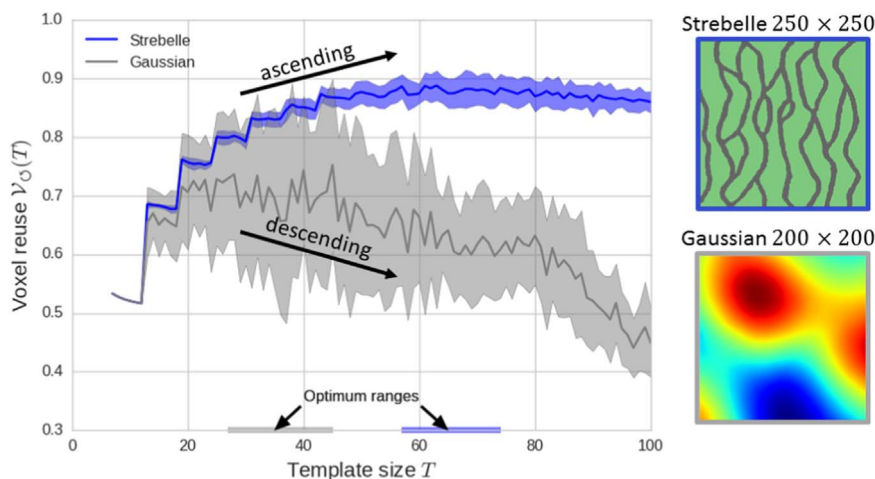
Fig. 28. Mean voxel reuse for Strebelle and Gaussian training images with ascending and descending trends, respectively. Optimum range for template size depicted in horizontal axis.

stationary random processes is error-free. Although we do not prove the result for non-stationary random processes where boundary cuts are also a function of space, we expect the error to be very low in practice.

This approximation with elementary overlapping paths cannot be extended to 3D random processes without errors in general. By following a similar derivation we can write

$$\mathbb{E}[\mathcal{V}_{\circleddash}] = a_0 + a_1 \mathbb{E}[\mathcal{V}_{\circleddash}^{xy}] + a_2\, \mathbb{E}[\mathcal{V}_{\circleddash}^{xz}] + \cdots + a_4\, \mathbb{E}[\mathcal{V}_{\circleddash}^{xyz}] \qquad (13)$$

which is the equation of a hyperplane defined by the normal vector $(a_1, a_2, a_3, a_4) \in \mathbb{R}_+^4$. This vector is a function of (m_x, m_y, m_z) and there are counter-examples where the maxima T^* is altered by the overlapping path size. If besides stationarity we assume that the training image is isotropic (i.e. statistics do not vary with direction), we have $\mathbb{E}[\mathcal{V}_{\circleddash}^{xy}] = \mathbb{E}[\mathcal{V}_{\circleddash}^{yz}] = \mathbb{E}[\mathcal{V}_{\circleddash}^{xz}] = \mathbb{E}[\mathcal{V}_{\circleddash}^{xyz}] = \mathbb{E}[\mathcal{V}_{\circleddash}^{\bar{\circleddash}}]$ and the approximation $\mathbb{E}[\mathcal{V}_{\circleddash}] = a_0 + (a_1 + a_2 + a_3 + a_4)\mathbb{E}[\mathcal{V}_{\circleddash}^{\bar{\circleddash}}]$ is error-free again.

We emphasize that the mean voxel reuse criterion is a function of both the training image and the quilting algorithm itself. To our knowledge, there is no other criterion with such property in the literature. In order to assess the robustness of the criterion, we perform a few basic checks with overhead shots of the flume experiment.

The first check consists of plotting the mean voxel reuse for different times of the experiment. In Fig. 27, we observe that the function is preserved across time with very small fluctuations. This result matches our expectation given that this is an autogenic deltaic system without external forcing that could alter the texture.

The second and last check consists of choosing a few template sizes T^h and T^l for which the mean voxel reuse is high and low, respectively. The criterion states that T^h leads to good texture reproduction in image quilting, whereas T^l does not. In Fig. 28, we illustrate the mean voxel reuse and optimum template ranges for the Strebelle and Gaussian training images. Fig. 22 was generated with $T^h = 63$ and $T^l = 12$, and Fig. 23 was generated with $T^h = 32$ and $T^l = 82$.

5. Conclusions

In this work, we proposed a systematic probabilistic procedure for data aggregation in MPS simulation. We implemented the procedure within image quilting and tested it on 2D process-based and 3D process-mimicking geological models. Our results show that the procedure is fast, dispenses fine parameter tuning, and produces realistically-looking realizations conditioned to auxiliary variables and hard data.

We introduced a novel criterion for template design that generalizes the Shannon entropy to continuous training images. The criterion is based on the concept of voxel reuse and is the first in the literature that

is quilting-aware. We proposed an efficient approximation of the mean voxel reuse and proved that it is error-free under stationary assumptions. We recognized artifacts in the image quilting realizations caused by complex landforms in 3D. These artifacts call for a better representation of incomplete patterns in the training image and should be seen as a current defect of the algorithm. Another limitation that deserves attention is that of suboptimal texture reproduction with dense hard data configurations. Our method can work with dense configurations, but may lead to suboptimal texture reproduction if speed is to be maintained. Future developments should be concentrated on these two fronts.

Another important issue that is not addressed in this work is that of data uncertainty. We assumed that both hard and soft data are free of errors. For applications where measurement errors are large, the proposed algorithm, like most other stochastic simulation algorithms mentioned in the paper, is not appropriate.

The accompanying software was made available as a Julia package. Documentation can be found online including examples of use and instructions for fast simulation with GPUs: https://github.com/juliohm/ImageQuilting.jl.

References

Abdollahifard, M.J., 2016. Fast multiple-point simulation using a data-driven path and an efficient gradient-based search. Comput. Geosci. 86, 64–74. http://dx.doi.org/10.1016/j.cageo.2015.10.010.

Allard, D., Comunian, A., Renard, P., 2012. Probability Aggregation Methods in Geoscience. 〈http://dx.doi.org/10.1007/s11004-012-9396-3〉.

Arpat, G.B., Caers, J., 2007. Conditional simulation with patterns. Math. Geol. 39, 177–203. http://dx.doi.org/10.1007/s11004-006-9075-3.

Borg, I., Groenen, P.J., 2005. Modern multidimensional scaling. Learning, vol. 40, 637. URL 〈http://www.springer.com/statistics/statistical+theory+and+methods/book/978-0-387-98134-5?cm_mmc=AD-_-Enews-_-ECS12245_V1-_-978-0-387-98134-5〉. 〈http://dx.doi.org/10.1007/0-387-28981-X〉. arXiv: 1011.1669v3.

Boykov, Y.Y., Jolly, M.P., 2001. Interactive graph cuts for optimal boundary & region segmentation of objects in ND images. In: Proceedings of the Eighth IEEE International Conference on Computer Vision. ICCV 2001, pp. 105–112. 〈http://dx.doi.org/10.1109/ICCV.2001.937505〉.

Boykov, Y., Kolmogorov, V., 2001. An experimental comparison of min-cut/max-flow algorithms for energy minimization in vision. In: Lecture Notes in Computer Science (including subseries Lecture Notes in Artificial Intelligence and Lecture Notes in Bioinformatics), pp. 359–374. 〈http://dx.doi.org/10.1007/3-540-44745-8_24〉. arXiv:0703101v1.

Briere, C., Giardino, A., Werf, J.J.V.D., 2004. Morphological modelling of bar dynamics with Delft3d: the quest for optimal free parameter settings using an automatic calibration technique. Coast. Eng., 2010, 1–12. ⟨http://dx.doi.org/10.9753/icce.v32.sediment.60⟩.

Chugunova, T.L., Hu, L.Y., 2008. Multiple-point simulations constrained by continuous auxiliary data. Math. Geosci. 40, 133–146. http://dx.doi.org/10.1007/s11004-007-9142-4.

Criminisi, A., Perez, P., Toyama, K., 2003. Object removal by exemplar-based inpainting. In: Proceedings of the IEEE Computer Vision and Pattern Recognition (CVPR). URL ⟨https://www.microsoft.com/en-us/research/publication/object-removal-by-exemplar-based-inpainting/⟩.

Deutsch, C.V., Tran, T.T., 2002. FLUVSIM: a program for object-based stochastic modeling of fluvial depositional systems. Comput. Geosci. 28, 525–535. http://dx.doi.org/10.1016/S0098-3004(01)00075-9.

Dubuisson, M.P., Jain, a.K., 1994. A modified Hausdorff distance for object matching. In: Proceedings of the 12th International Conference on Pattern Recognition, 1, 566–568. ⟨http://dx.doi.org/10.1109/ICPR.1994.576361⟩.

Efros, A., Freeman, W., 2001. Image quilting for texture synthesis and transfer. In: Proceedings of the 28th Annual Conference on Computer Graphics and Interactive Techniques, 1–6, URL ⟨http://dl.acm.org/citation.cfm?id=383296⟩. ⟨http://dx.doi.org/10.1145/383259.383296⟩.

El Ouassini, A., Saucier, A., Marcotte, D., Favis, B.D., 2008. A patchwork approach to stochastic simulation: a route towards the analysis of morphology in multiphase systems. Chaos Solitons Fractals 36, 418–436. http://dx.doi.org/10.1016/j.chaos.2006.06.100.

Elias, E.P.L., Walstra, D.J.R., Roelvink, J.a., Stive, M.J.F., Klein, M.D., 2001. Hydrodynamic validation of Delft3D with field measurements at Egmond. Coast. Eng. 40549, 2714–2727. http://dx.doi.org/10.1061/40549(276)212, (URL ⟨http://ascelibrary.org/doi/abs/10.1061/40549(276)212⟩)(2000).

Faucher, C., Saucier, A., Marcotte, D., 2014. Corrective pattern-matching simulation with controlled local-mean histogram. Stoch. Environ. Res. Risk Assess. 28, 2027–2050. http://dx.doi.org/10.1007/s00477-014-0864-9.

Giri, S., Vuren, S.V., Ottevanger, W., Sloff, K., 2008. A preliminary analysis of bedform evolution in the Waal during 2002–2003 flood event using Delft3D. Mar. River Dune Dyn., 141–148.

Høyer, A.S., Jørgensen, F., Sandersen, P.B.E., Viezzoli, A., Møller, I., 2015. 3D geological modelling of a complex buried-valley network delineated from borehole and AEM data. J. Appl. Geophys. 122, 94–102. http://dx.doi.org/10.1016/j.jappgeo.2015.09.004.

Honarkhah, M., Caers, J., 2010. Stochastic simulation of patterns using distance-based pattern modeling. Math. Geosci. 42, 487–517. http://dx.doi.org/10.1007/s11004-010-9276-7.

Huttenlocher, D.P., Klanderman, G.A., Rucklidge, W.J., 1993. Comparing images using the Hausdorff distance. IEEE Trans. Pattern Anal. Mach. Intell. 15, 850–863. http://dx.doi.org/10.1109/34.232073.

Journel, A.G., Deutsch, C.V., 1993. Entropy and spatial disorder. Math. Geol. 25, 329–355. http://dx.doi.org/10.1007/BF00901422.

Journel, A.G., 2002. Combining knowledge from diverse sources: an alternative to traditional data independence hypotheses. Math. Geol. 34, 573–596. http://dx.doi.org/10.1023/A:1016047012594.

Kim, W., Sheets, B.A., Paola, C., 2010. Steering of experimental channels by lateral basin tilting. Basin Res. 22, 286–301. http://dx.doi.org/10.1111/j.1365-2117.2009.00419.x.

Kwatra, V., Schodl, A., Essa, I., Turk, G., Bobick, A., 2003. Graphcut textures: image and video synthesis using graph cuts. ACM Trans. Graph. 22, 277–286. http://dx.doi.org/10.1145/882262.882264.

Lesser, G.R., Roelvink, J.A., van Kester, J.A.T.M., Stelling, G.S., 2004. Development and validation of a three-dimensional morphological model. Coast. Eng. 51, 883–915. http://dx.doi.org/10.1016/j.coastaleng.2004.07.014.

Lopez S., Cojan I., Rivoirard J., G.A., 2008. Process-based stochastic modelling: meandering channelized reservoirs. Spec. Publ. International Assoc. Sedimentol., 40, 139:144.

Lopez, S., 2003a. Channelized Reservoir Modeling: A Stochastic Process-based Approach (Theses). {É}cole Nationale Sup{é}rieure des Mines de Paris, (URL ⟨https://pastel.archives-ouvertes.fr/pastel-00000630⟩).

Lopez, S., 2003b. Modélisation de réservoirs chenalisés méandriformes: une approche génétique et stochastique (Ph.D. thesis). Centre de Geostatistique.

Maharaja, A., 2008. TiGenerator: object-based training image generator. Comput. Geosci. 34, 1753–1761. http://dx.doi.org/10.1016/j.cageo.2007.08.012.

Mahmud, K., Mariethoz, G., Caers, J., Tahmasebi, P., Baker, A., 2014. Simulation of Earth textures by conditional image quilting. Water Resour. Res. 50, 3088–3107. http://dx.doi.org/10.1002/2013WR015069.

Mariethoz, G., Caers, J., 2014. Multiple-point Geostatistics: Stochastic Modeling with Training Images. ⟨http://dx.doi.org/10.1002/9781118662953⟩.

Mariethoz, G., Renard, P., Straubhaar, J., 2010. The direct sampling method to perform multiple-point geostatistical simulations. Water Resour. Res., 46. http://dx.doi.org/10.1029/2008WR007621.

Matheron, G., 1963. Principles of geostatistics. Econ. Geol. 58, 1246–1266. http://dx.doi.org/10.2113/gsecongeo.58.8.1246.

Paola, C., Straub, K., Mohrig, D., Reinhardt, L., 2009. The "unreasonable effectiveness" of stratigraphic and geomorphic experiments. Earth-Sci. Rev. 97, 1–43. http://dx.doi.org/10.1016/j.earscirev.2009.05.003.

Paola, C., Twilley, R.R., Edmonds, D.A., Kim, W., Mohrig, D., Parker, G., Viparelli, E., Voller, V.R., 2011. Natural processes in delta restoration: application to the Mississippi Delta. Ann. Rev. Mar. Sci. 3, 67–91. http://dx.doi.org/10.1146/annurev-marine-120709-142856, (URL ⟨http://www.ncbi.nlm.nih.gov/pubmed/21329199⟩).

Paola, C., 2000. Quantitative Models of Sedimentary Basin Filling. ⟨http://dx.doi.org/10.1046/j.1365-3091.2000.00006.x⟩.

Renard, P., Allard, D., 2013. Connectivity metrics for subsurface flow and transport. Adv. Water Resour. 51, 168–196, (URL ⟨http://dx.doi.org/10.1016/j.advwatres.2011.12.001⟩).

Sørense, K., Auken, E., 2004. SkyTEM ? A new high-resolution helicopter transient electromagnetic system. Explor. Geophys. 35, 194. http://dx.doi.org/10.1071/eg04194, (URL ⟨https://doi.org/10.1071%2Feg04194⟩).

Scheidt, C., Fernandes, A.M., Paola, C., Caers, J., 2015. Can Geostatistical Models Represent Nature's Variability? An Analysis Using Flume Experiments. AGU Fall Meeting Abstracts.

Scheidt, C., Fernandes, A.M., Paola, C., Caers, J., 2016. Quantifying natural delta variability using a multiple-pointgeostatistics prior uncertainty model. J. Geophys. Res.: Earth Surf., 1–19, (⟨http://dx.doi.org/10.1002/2016JF003922.Received⟩).

Straub, K.M., Paola, C., Mohrig, D., Wolinsky, M.a., George, T., 2009. Compensational stacking of channelized sedimentary deposits. J. Sediment. Res. 79, 673–688. http://dx.doi.org/10.2110/jsr.2009.070.

Strebelle, S., 2002. Conditional simulation of complex geological structures using multiple-point statistics. Math. Geol. 34, 1–21. http://dx.doi.org/10.1023/A:1014009426274.

Tahmasebi, P., Sahimi, M., 2012. Reconstruction of three-dimensional porous media using a single thin section. Phys. Rev. E 85, 1–13. http://dx.doi.org/10.1103/PhysRevE.85.066709.

Tahmasebi, P., Hezarkhani, A., Sahimi, M., 2012. Multiple-point geostatistical modeling based on the cross-correlation functions. Comput. Geosci. 16, 779–797. http://dx.doi.org/10.1007/s10596-012-9287-1.

Tahmasebi, P., Sahimi, M., Caers, J., 2014. MS-CCSIM: accelerating pattern-based geostatistical simulation of categorical variables using a multi-scale search in Fourier space. Comput. Geosci. 67, 75–88. http://dx.doi.org/10.1016/j.cageo.2013.03.009.

Tal, M., Paola, C., 2010. Effects of vegetation on channel morphodynamics: results and insights from laboratory experiments. Earth Surf. Process. Landf. 35, 1014–1028. http://dx.doi.org/10.1002/esp.1908.

Thomsen, R., Søndergaard, V.H., Sørensen, K.I., 2004. Hydrogeological mapping as a basis for establishing site-specific groundwater protection zones in Denmark. Hydrogeol. J. 12, 550–562. http://dx.doi.org/10.1007/s10040-004-0345-1.

Xu, S., 2014. Integration of Geomorphic Experiment Data in Surface-Based Modeling: From Characterization To Simulation.

Yang, L., Hou, W., Cui, C., Cui, J., 2016. GOSIM: a multi-scale iterative multiple-point statistics algorithm with global optimization. Comput. Geosci. 89, 57–70. http://dx.doi.org/10.1016/j.cageo.2015.12.020.

Zhang, T., Switzer, P., Journel, A., 2006. Filter-based classification of training image patterns for spatial simulation. Math. Geol. 38, 63–80. http://dx.doi.org/10.1007/s11004-005-9004-x.

Zhang, T., Du, Y., Huang, T., Yang, J., Li, X., 2015. Stochastic simulation of patterns using ISOMAP for dimensionality reduction of training images. Comput. Geosci. 79, 82–93. http://dx.doi.org/10.1016/j.cageo.2015.03.010.